International Journal of Nanomedicine

Dovepress

open access to scientific and medical research

Open Access Full Text Article

ORIGINAL RESEARCH

Facile Synthesis of Melanin-Dye Nanoagent for NIR-II Fluorescence/Photoacoustic Imaging-Guided Photothermal Therapy

This article was published in the following Dove Press journal:
International Journal of Nanomedicine

Jinghua Sun[1,*]
Wenwen Cai[1,*]
Yao Sun[2,*]
Chunyan Guo[1]
Ruiping Zhang[1]

[1]Center for Translational Medicine Research, Shanxi Medical University, Imaging Department, The Affiliated Bethune Hospital of Shanxi Medical University, Taiyuan 030001, People's Republic of China; [2]Key Laboratory of Pesticides and Chemical Biology, Ministry of Education, College of Chemistry, Central China Normal University, Wuhan 430079, People's Republic of China

*These authors contributed equally to this work

Background: Laryngeal cancer is the second most common type of primary epithelial malignant tumor in the head and neck region, and the development of therapies that are more precise, efficient, and safe is necessary to preserve patient speech and swallowing functions as much as possible. Multi-modal imaging-guided photothermal therapy (PTT) can precisely delineate tumors, monitor the real-time accumulation of photothermal agents at the tumor site, accurately select the optimal region for irradiation, and predict the best time for laser treatment. Compared with exogeneous photothermal agents, endogenous melanin materials have better biosafety in vivo, in terms of native biocompatibility and biodegradability, as well as good near-infrared (NIR) absorbance. An NIR-II dye can be attached to melanin via a facile method, and applying a melanin-dye-based nanoprobe could be an excellent choice for the elimination of superficial laryngeal cancer while avoiding total laryngectomy.

Methods: In this work, a promising nanoprobe was constructed using a facile EDC/NHS strategy involving an NIR-II dye and melanin nanoparticles.

Results: The nanoprobe exhibited good water solubility, dispersibility, strong NIR-II fluorescence and photoacoustic (PA) signals, and higher photothermal performance. Cellular studies showed that the nanoprobe had low toxicity, excellent biocompatibility, and significantly enhanced imaging properties. After the nanoprobe was intravenously injected into Hep-2 laryngeal xenografts, superior dual-modal images were obtained at various time points, which revealed that the optimal photothermal treatment time was 8 h. Subsequently, PTT was carried out in vivo, and laryngeal tumors were completely eliminated after laser irradiation without any obvious side effects.

Conclusion: These results indicate the immense potential of nanoprobes for the NIR-II fluorescence/PA imaging-guided photothermal therapy of laryngeal cancer.

Keywords: melanin, small molecular fluorescence dye, NIR-II fluorescence imaging, photoacoustic imaging, photothermal therapy, laryngeal cancer

Introduction

Fluorescence imaging has received considerable attention in the biomedical field, as it facilitates real-time and noninvasive detection with higher sensitivity and superior specificity.[1] However, the living imaging capacity in the traditional near-infrared-I (NIR-I, 700–900 nm) has been greatly restricted due to its limited penetration. A novel fluorescence imaging approach in the second NIR window (NIR-II, 1000–1700 nm) provides deeper tissue penetration (~10 mm), a higher signal-to-noise ratio, and better spatial resolution than NIR-I because of minimal photon

Correspondence: Ruiping Zhang,
Email zrp_7142@sxmu.edu.cn

scattering and tissue autofluorescence.[2] Recent studies, including those regarding the detection of metastatic lymph nodes,[3] tumor and vessel imaging,[4–6] and intraoperative guidance,[7,8] have shown that biological imaging advantages significantly improves as wavelengths increase. Thus far, quantum dots,[9–11] carbon nanotubes,[12,13] rare earth-doped nanoparticles,[14,15] squaraine dyes,[16,17] semiconducting polymer nanoparticles,[18] and small-molecule dyes[5,19,20] have all been actively used for NIR-II imaging. The recent rapid development of small molecule dyes, in particular, has led to the use of effective probes for NIR-II fluorescence bioimaging. Zhang et al achieved high-resolution dynamic imaging of vascular changes particular to a model of traumatic brain injury using the small-molecule dye, IR-E1.[21] Osteosarcoma and lung metastasis can also be visualized through two homologous types of small-molecule NIR-II fluorescent probes.[22] Furthermore, previous works by our research group explored the use of a series of fluorophores for tumor imaging and imaging-guided therapy.[20,23–25]

Although small-molecule dyes have high quantum yields and good NIR absorbance,[25–27] their low solubility, quick clearance, and toxicity restrict their application.[19,27] In recent years, the rapid development of nanotechnology has provided potential solutions to the above problems. In particular, the introduction of a nanocarrier might not only mitigate the poor water solubility and short circulation time, but also facilitate the integration of diagnosis and treatment.[28–31] Thus, the exploitation of efficient, modifiable, and biologically nano-carriers that can overcome the defects of small-molecular dyes would be highly beneficial for developing precise therapies. Compared with exogeneous nanocarriers, endogenous biomaterials from living organisms have better biosafety in vivo. Melanin, an endogenous biopolymer that exists in most organisms, has attracted much attention for biomedical application attributing to its interesting properties, including natural biocompatibility and biodegradability, good NIR absorbance, strong metal ion chelation, anti-oxidant properties, and so forth.[32] In our previous work, we synthesized ultrasmall water-soluble melanin nanoparticles (MNP) that preserve many of the beneficial properties of natural melanin.[33–36] Moreover, MNP can be easily modified by facile methods. $C_{56}H_{42}N_4O_{12}S_4$ (H2, molecular weight:1091.21), a hydrophobic organic small molecule-dye, emits strong NIR-II fluorescence at about 1000 nm and has an NIR absorbance peak at around 750 nm, but its solubility limits biological application. The design and construction of a nanoprobe based on melanin nanoparticles and the NIR-II dye H2 wound be extremely useful for image-guided tumor therapy.

Traditional radiotherapy and chemotherapy for laryngeal cancer, which is the second most frequent malignant tumor of epithelia in the head and neck region, have severe side effects.[37,38] Photothermal therapy (PTT) is a novel and non-invasive method that uses photo-absorbers to convert light energy into thermal energy to destroy tumor cells. PTT is highly specific, great efficiency, easy to operate, and has few side effects.[39,40] Especially, imaging-guided PTT, which can precisely delineate tumor, monitor the accumulation procedure of nano-agents in the tumor, select the most appropriate irradiation region, and determine the optimal timing of laser treatment,[33,41–43] therefore, it seems to be the best choice for eliminating laryngeal cancer without a total laryngectomy. NIR-II fluorescence imaging has a higher sensitivity and deeper tissue penetration ability than traditional optical imaging technique. However, a single-modality imaging technique usually provides insufficient information. Photoacoustic imaging (PAI) is an emerging optical imaging method in which photon energy is absorbed and converted into acoustic waves, which are then detected using ultrasound.[44] It has great potential for noninvasive deep-tissue visualization with higher spatial resolution and stronger optical contrast than conventional optical and ultrasound imaging method.[45] Moreover, through the use of ultrasound, PA imaging can simultaneously provide anatomical and molecular imaging in real-time.[46] Considering the superior and complementary performance of NIR-II fluorescence imaging and PAI, integrating the merits of these two imaging modalities is particularly appealing when aiming to achieve precise cancer diagnosis and imaging-guided therapy.[47]

In this study, we synthesized a novel nanoprobe, MNPH2, by combining melanin nanoparticles with a small-molecule dye, H2, via a one-step EDC/NHS reaction, for the NIR-II fluorescence/PA imaging-guided PTT of laryngeal cancer (Figure 1). The solubility and biocompatibility of H2 significantly improved after it was integrated with MNP, and H2 endowed MNP with NIR-II fluorescence. Moreover, the increase of NIR absorbance in MNP also enhanced the overall performance of PAI and PTT. Additionally, the nanoprobe displayed good solubility, stability, biocompatibility, dual-modal imaging, and a strong photothermal performance. After intravenous injection, NIR-II fluorescence and PA imaging results indicated that

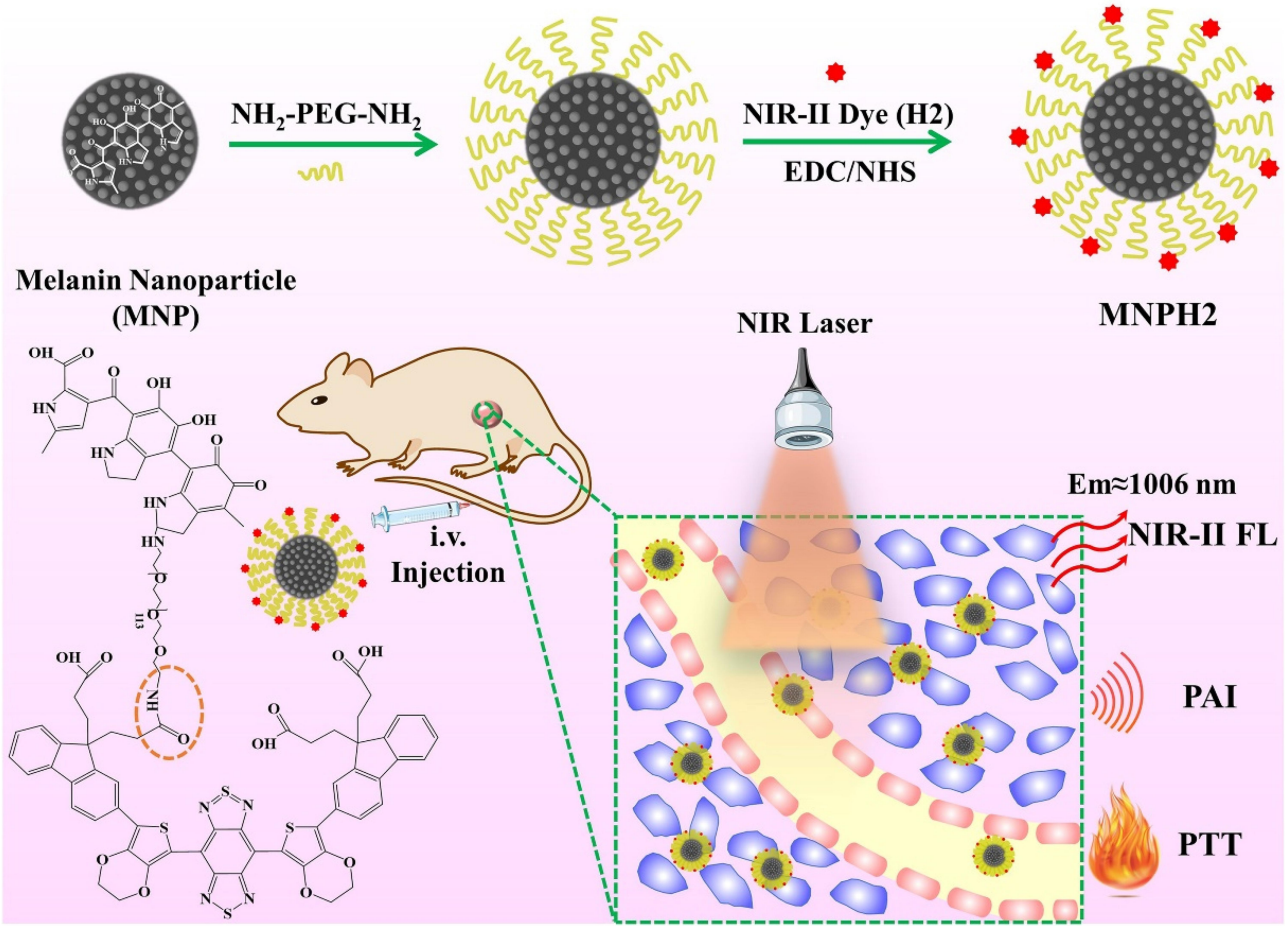

Figure 1 Schematic illustration of the MNPH2 preparation and theranostic application for NIR-II fluorescence/PA dual-modal imaging-guided PTT of laryngeal carcinoma.

the MNPH2 nanoprobe effectively accumulated at the tumor site, and the optimal photothermal treatment time was 8 h. Eventually, the tumor was effectively ablated after it was irradiated with an NIR laser, and no obvious side effects were seen. Therefore, the MNPH2 nanoprobe has immense potential for use in NIR-II fluorescence/PA dual-modal image-guided PTT of laryngeal cancer in vivo.

Materials and Methods

Materials

Melanin, propidium iodide (PI), and calcein acetoxymethyl ester (Calcein-AM) were obtained from Sigma-Aldrich. The NIR-II organic small-molecule dye H2 was supplied from Central China Normal University. Sodium hydroxide (NaOH) and hydrochloric acid (37 wt% HCl) were bought from Sinopharm Chemical Reagent Beijing Co., Ltd. Amine-PEG-amine (NH2-PEG-NH2, 5 kDa) was purchased from Shanghai Zzbio Co., Ltd. N-hydroxysuccinimide (NHS) and 1-ethyl-3-(3-dimethylaminopropyl) carbodiimide, hydrochloride (EDC) were obtained from Energy Chemical (Shanghai, China). N, N'-dimethylformamide (DMF) was obtained from Alfa Aesar (Acros, Belgium, France). Triethylamine was purchased from Shentai chemical reagent co. LTD (Tianjin, China). Phosphate buffer saline (PBS) and 4,6-diamidino-2-phenylindole (DAPI) were gained from Boster Biological Technology Co., Ltd. CCK-8 kit was purchased from DOJINDO Molecular Technologies, Inc. (Shanghai, China). Dulbecco's Modified Eagle's Medium (DMEM), fetal bovine serum (FBS), penicillin/streptomycin, and trypsin solution were all obtained from Gibco (America).

Preparation and Characterization of MNPH2

The water-soluble melanin nanoparticles (MNP) were prepared via ultrasonication, and then were modified by NH_2-

PEG_{5000}-NH_2 according to the previous work.[33,36,48] The hydrophobic NIR-II fluorescence dye H2 with four carboxyl groups could be easily conjugated with amine groups of the PEGylated MNP via the EDC/NHS reaction. Briefly, H2 (0.4 mg), EDC (2 mg), and NHS (2 mg) were co-dissolved in DMF (2 mL) and magnetically stirred for 3 h to activate carboxyl groups. Then, the PEGylated MNP (1 mg/mL) was added in the above mixture solution. Subsequently, triethylamine was quickly dropped to adjust the pH to 7–8. The mixture was vigorously stirred at room temperature overnight. The final product labeled as MNPH2 was transferred into a 3500D dialysis membrane against deionized (DI) water for 48 h and concentrated with an ultrafiltration centrifuge filter (MWCO = 30 kD, Millipore) at 3500 rpm/min for 10 min to remove the excess substance.

The chemical binding between the PEGylated MNP (MNP-PEG) and dye H2 was analyzed by an iS50 Fourier-transform infrared (FTIR) spectrometer. JEM-2100F transmission electron microscopy (TEM, JEOL, Tokyo, Japan) was used to characterize the morphology and size of MNPH2. Hydrodynamic diameter and zeta potential were measured by a commercial dynamic light scattering spectrometers (DLS, Zetasizer Nano ZS90; Malvern Instruments, Malvern, UK). The absorption spectra of H2 in DMF, MNP and different concentrations (40, 60, 80, 100 μg/mL) of MNPH2 were determined by a UV–vis–NIR spectrophotometer (UV-6100; MAPADA Instruments, Shanghai, China). MNPH2 solutions (20 μL) were separately incubated with 150 μL of PBS, high-glucose DMEM medium, and fetal bovine serum (FBS) for 48 h to evaluate the physiological stability of MNPH2.

Imaging and Photothermal Performance of MNPH2

NIR-II fluorescence emission spectrum of MNPH2 triggered by a 785 nm laser beam was measured by an NS1 NanoSpectralyzer (Applied Nano Fluorescence, Houston, America). The excitation and emission spectra of MNPH2 in the UV-vis-NIR-I region were also determined by a fluorescence spectrometer. The fluorescence quantum yield (QY) of H2 and MNPH2 were calculated using IR-1061 in dichloromethane (QY=1.7%) as reference. In a standard manner, a series of solutions of IR-1061 in dichloromethane, H2 in THF and MNPH2 in deionized water were tested and the integrated fluorescence was plotted against absorbance for IR-1061, H2 and MNPH2. MNPH2 with various concentrations (200, 100, 50, 25, 12.5, 6.25 μg/mL) were added to Eppendorf tubes (200 μL) and orderly arranged in an NIR-II Fluorescence In Vivo Imaging System (Suzhou NIR-Optics Technological Co., Ltd., Suzhou, China). DI water was set as a control. After irradiated by an 808 nm built-in laser, the images of NIR-II fluorescence signals passed through a 1000 nm filter were captured. PA contrast performances of MNPH2 solutions in different concentrations of 400, 200, 100, 50, 25, 12.5, 6.25, and 0 μg/mL were performed in multispectral optoacoustic tomographic platform (MSOT inSight 128, iThera Medical GmbH, Munich, Germany) under pulse laser (680–980 nm). After reconstruction and analysis of the obtained MSOT images, the linear relationship was fitted by analyzing regions-of-interest of these images.

To assess the photothermal performance, MNPH2 aqueous solutions with various concentrations (200, 100, 50, 25, 12.5, 0 μg/mL) placed into 200 μL tubes were irradiated by an 808 nm laser at 0.5 W/cm^2 for 5 min. Meanwhile, 100 μg/mL of MNPH2 aqueous solution was irradiated at different laser power densities of 0.25, 0.5, 0.75, and 1.0 W/cm^2 for 5 min. Thermal images and temperature changes were monitored every 30 s by an infrared thermal imaging camera (Ti400). To obtain the heating and cooling curve, the MNPH2 solution (100 μg/mL) was irradiated with a laser (808 nm, 0.5 W/cm^2). When a stable maximum temperature was reached, the laser was turned off and the solution was subsequently cooled to room temperature. DI was used as a control. The photothermal conversion efficiency of the MNPH2 was calculated as following:[49]

$$\eta = \frac{hs(T_{max} - T_{surr}) - Q_{dis}}{I\left(1 - 10^{-A}\right)} = \frac{mc(T_{max} - T_{surr}) - Q_{dis}}{\tau_s I\left(1 - 10^{-A}\right)} \quad (1)$$

The photothermal conversion efficiency η can be obtained from Eq.1. Where "h" is the heat transfer coefficient, "s" is the surface area of the container. "T_{max}" and "T_{surr}" represent the initial and the highest temperature. "I" is the power of laser and "A" is the absorbance at 808 nm. "Q_{dis}" expresses heat dissipated from the light absorbed by the solvent and container. "m" represents the quality of MNPH2 solution. "c" is the specific heat capacity of water. The value of τ_s was obtained from Eq.2.

$$\tau_s = -t/\ln\theta \quad (2)$$

"θ" is the dimensionless driving force and "t" is the corresponding time. In order to test the photostability of MNPH2, 100 μg/mL MNPH2 aqueous solution was irradiated at an interval of 5 min and sustained six laser on/off cycling.

Cell Experiments

Cell Culture

The human laryngeal cancer Hep-2 cell line was purchased from the Type Culture Collection of the Chinese Academy of Sciences (Shanghai, China). Hep-2 cells (human laryngeal squamous cell carcinoma) were incubated in high-glucose DMEM medium containing 10% fetal bovine serum (FBS) and 1% antibiotics (penicillin-streptomycin) at 37 °C within in a humidified standard incubator (5% CO_2).

Cytotoxicity Assessments in vitro

The cell viability of MNPH2 was assessed by a standard CCK-8 kit. Hep-2 cells (1×10^4 cells per well) were seeded into 96-well plates overnight until attachment. Then the cells were co-incubated with 100 μL culture medium containing MNPH2 of various concentrations (800, 400, 200, 100, 50, 25, 12.5, 6.25, 0 μg/mL) for 24 h. Afterward, the old medium was removed and rinsed with PBS. Finally, each well was added 100 μL fresh medium containing 10 μL of CCK-8 followed by another 2 h of incubation and measured the absorbance by an Epoch 2 Microplate reader (BioTek, Vermont, America) at 450 nm.

Cell Imaging and Uptake Analysis

To verify the cellular imaging and uptake behaviors of MNPH2, Hep-2 cells were examined using NIR-II fluorescence Microscope (Suzhou NIR-Optics Co., Ltd., Suzhou, China), MOST system and confocal laser scanning microscopy (CLSM, FV1000, Olympus, Tokyo, Japan). In brief, Hep-2 cells with a density of 1×10^5 cells were seeded in a glass-bottomed dish with a diameter of 20 mm. After attachment, the old medium was replaced with fresh medium containing MNPH2 (100 μg/mL) and cultured for 4 h. Then the medium was discarded and Hep-2 cells were gently rinsed with PBS buffer and fixed with 4% paraformaldehyde. Subsequently, Hep-2 cells were observed by NIR-II fluorescence Microscope and MOST imaging system. After stained by 4′, 6-diamidino-2-phenylindole (DAPI), Hep-2 cells were further studied by CLSM. The excitation of DAPI was at 360 nm, while MNPH2 was at 457 nm and 785 nm.

Photothermal Cytotoxicity in vitro

In vitro photothermal performance was evaluated also by CCK-8 assay. Specifically, the cells were seeded to 96-well plates with a concentration of 10^4 cells per well. After 24 h, the culture media were removed and the cells were washed by PBS. Then, fresh culture media containing the MNPH2 with different concentrations (800, 400, 200, 100, 50, 25, 12.5, 6.25, 0 μg/mL) were co-incubated 12 h. Subsequently, the cells were irradiated by an NIR laser at a power density of 0.75 W/cm^2 for 5 min. After that, cell viability was analyzed. To further evaluate the photothermal ablation on cancer cells induced by MNPH2, Hep-2 cells treated with different methods were dyed with Calcein-AM/PI Double Stain. Hep-2 cells with a density of 1.5×10^4 cells were seeded in a 96-well plate to grow overnight. After attachment, the culture medium was replaced with MNPH2 culture medium (100 μg/mL) for 12 h. Then the cells were irradiated with or without 808 nm laser at a power density of 0.75 W/cm^2 for 5 min. Hep-2 cells treated with no-MNPH2 culture medium were set as a control. After that, the cells were stained with Calcein-AM and PI to outline live and dead cells, respectively. Eventually, the images were captured by a fluorescence microscope (OLYMPUS, IX73).

Animal Model

All animal procedures were performed in accordance with the Guidelines for Institutional Animal Care and Use Committee and approved by the Animal Ethics Committee of Shanxi Medical University (No. SYDL2019002). Female BALB/c nude mice (6–8 weeks) with bodyweight of 18–20 g were purchased from Beijing Vital River Laboratory Animal Technology Co. Ltd. BALB/c nude mice were kept under standard housing condition before use. Hep-2 cells (50 μL PBS containing 2.0×10^6 cells) were subcutaneously implanted on the dorsum region of the right leg to generate tumor-bearing nude mice. When the tumors reached about 100 mm^3, these nude mice were conducted for imaging and therapy studies.

NIR-II Fluorescence /PA Imaging in vivo

NIR-II Fluorescence In Vivo Imaging System is a kind of noninvasive whole-body imaging technique. In this experiment, 200 μL MNPH2 aqueous solution (800 μg/mL) was also intravenously injected into tumor-bearing nude mice. The mice (n=3) were kept in anesthesia state using

isoflurane mixed with oxygen and excited by an 808 nm internal laser at a power of 2.0 W and exposure time of 100 ms. The images collection time was set at pre-injection, 2, 4, 8, 12, and 24 h post intravenous injection of MNPH2. The fluorescence intensities of NIR-II images were analyzed using the software Image J. To verify the biodistribution and accumulation performance of MNPH2 in vivo, the tumor-bearing mice were sacrificed at 24 h after imaging and major tissues including heart, liver, spleen, lung, kidney, and tumor were imaged, and the signal intensities were quantitatively analyzed.

For in vivo PA imaging, Hep-2 tumor-bearing nude mice (n=3) were intravenously injected with 200 μL MNPH2 aqueous solution (800 μg/mL) via the tail vein. The above MSOT platform was conducted to obtain images of tumor regions at pre-injection, 2 h, 4 h, 8 h, 12 h, and 24 h post injection. The NIR excitation wavelength of MSOT scanner consists of a range of 680–980 nm. Besides, the PA signal intensities of tumor site at different points were also quantitatively analyzed.

In vivo PTT

The photothermal effects of MNPH2 were studied in vivo. Once the mean tumor volume reached approximately 100 mm^3, Hep-2-bearing nude mice were randomly divided into four groups (n=3): (1) PBS only, (2) PBS + Laser, (3) MNPH2 only, and (4) MNPH2 + Laser. After intravenous injection of MNPH2 aqueous solution (200 μL, 800 μg/mL) or PBS (200 μL) into the mice, the tumors were irradiated under 808 nm laser at a power density of 1.0 W/cm^2 for 5 min. During the irradiation, the thermal images and changes in temperature were recorded by an infrared thermal camera. Besides, relative tumor volumes and body weights of mice were simultaneously recorded after treatment. To investigate the photothermal efficacy, the tumors were harvested and stained with H&E (Hematoxylin and Eosin) for histopathological analysis.

Biosafety Assessment

To explore the potential side effects, healthy mice (n=3) were intravenously injected with 200 μL MNPH2 aqueous solution (2 mg/mL) and PBS, respectively. After sacrificed, serum levels of aspartate aminotransferase (AST), alanine aminotransferase (ALT), serum creatinine (Scr), and blood urea nitrogen (BUN) were measured to assess the liver and renal function. Meanwhile, major organs including heart, liver, spleen, lung, and kidney were harvested and dealt with H&E staining. Blood was obtained from the mice and divided into experimental and control group. Experimental group was added with 50 μL MNPH2 solutions (200 μg/mL), and the control group was added with the same amount of saline. After standing for 2 h, the blood was centrifugated at 3000 rpm/min for 10 min, then the hemolysis photos were captured.

Statistical Analysis

All statistical analyses were performed using SPSS 22.0 software. Data were presented as mean ± SD. Means were compared using *t*-tests, a 95% confidence level was chosen to determine the significance between groups, and $p<0.05$ was considered as statistically significant.

Results and Discussion

Preparation and Characterization of MNPH2

The PEGylated melanin nanoparticles (MNP-PEG) were prepared using our previously reported methods.[33] As the number of free amino has been calculated to be 22 per MNP, the number of H2 molecules per MNP was 22, each of which contains excessive carboxyl groups. The nanoprobe MNPH2 was easily acquired via the EDC/NHS reaction between the $-NH_2$ of MNP-PEG and -COOH of H2. The success of the chemical bonding was verified by FT-IR spectra (Figure 2A), as characteristic absorption peaks at 2920 cm^{-1} in MNPH2 belong to the asymmetric C-H bond vibration of the H2 molecule. Furthermore, the weak absorption peaks at about 1690 cm^{-1} in MNPH2 represented amide I and result from stretching vibrations of the C=O groups.[50,51] Absorbance peaks for MNP-PEG were also observed within the MNPH2 spectrum, proving the success of the EDC/NHS reaction. The diameter and morphology of MNPH2 in aqueous solution were characterized by TEM and DLS. The TEM image of MNPH2 revealed a uniform size and good dispersity with an average diameter of about 21 nm (Figure 2B). The hydrodynamic diameter was approximately 25 nm (Figure 2C), and the larger particle size in DLS is likely to be their swelling of the hydrated particle. There was no precipitation or separation in the tubes after incubation with a different medium for 48 h, suggesting the nanoprobe has excellent solubility and physiological stability (Figure S1). The slight negative charge potential (−13.3 mV) of MNPH2 enabled a prolonged retention time, good stability

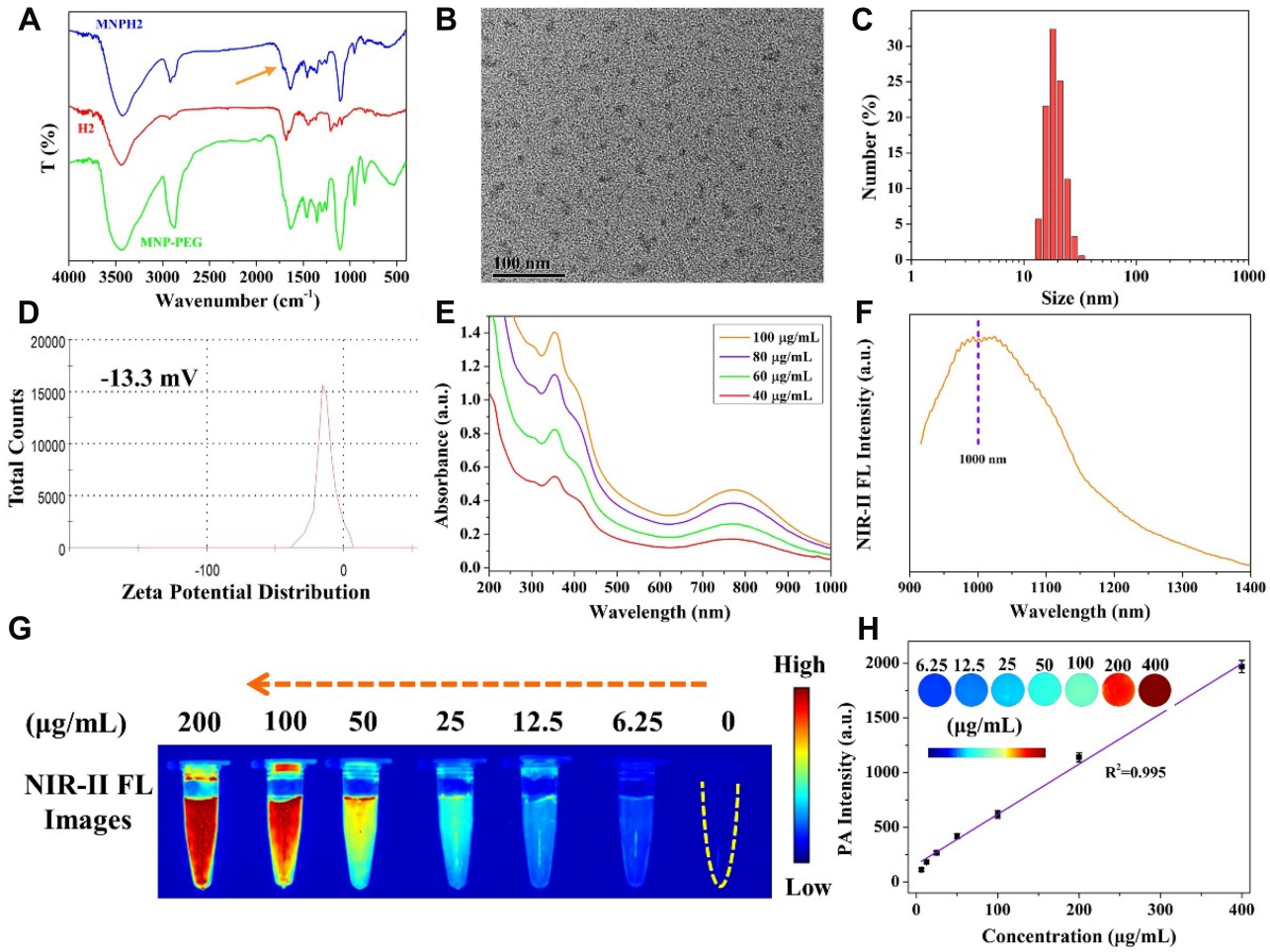

Figure 2 Characterization of MNPH2. (**A**) FT-IR spectra of MNP-PEG, H2, and MNPH2. (**B**) TEM image of MNPH2. (**C**) DLS analysis of the hydration size distribution of MNPH2. (**D**) Zeta potential of MNPH2. (**E**) UV-vis-NIR absorbance spectra of MNPH2 with different concentrations (40, 60, 80, and 100 μg/mL). (**F**) NIR-II fluorescence emission spectrum of MNPH2 upon 785 nm excitation. (**G**) NIR-II fluorescence images of MNPH2 with varying concentrations ranging from 0 to 200 μg/mL. (**H**) The linear relationship between concentrations and PA signals of MNPH2 (R^2=0.995). Inset presented PA images of MNPH2 with different concentrations.

in vivo, and enhanced permeability and retention effect[52] (Figure 2D).

The UV-vis-NIR absorption spectra of MNP-PEG in solution exhibited a monotone decreasing trend, while that of H2 had an obvious absorption peak at ~745 nm in DMF (Figure S2). The final nanoprobe MNPH2 displayed the characteristic absorptions of MNP-PEG and H2, further confirming the successful connection between MNP-PEG and H2. Additionally, the absorption performance of MNPH2 significantly improved in the NIR-I region with the introduction of H2, which is beneficial for PTT and PAI. The UV-vis-NIR spectra of MNPH2 of different concentrations (40, 60, 80, 100 μg/mL) are shown in Figure 2E. The absorbance intensity was gradually enhanced with increasing concentrations of MNPH2, which suggested it could be used as an agent for photothermal conversion and photoacoustic imaging.

The fluorescence spectra of MNPH2 in both the visible and NIR-II region were investigated. The excitation and emission spectra in the visible region are shown in Figure S3. The emission peak of MNPH2 was located at 609 nm under the maximum excitation wavelength of 457 nm. As shown in Figure 2F, the NIR-II fluorescence emission spectra based on a sensitive system showed a peak at 1006 nm and extended well into the NIR-II region under 785 nm excitation. Regarding the NIR-II fluorescence performance of MNPH2, fluorescence images showed that the brightness and signal intensities increased with increasing MNPH2 concentrations in aqueous solution (Figure 2G). The quantum yields of H2 in DMF and MNPH2 in DI were determined to be 0.63% and 0.20%, respectively, using IR-1061 in dichloromethane (QY = 1.7%) as a reference (Figure S4). The low quantum yield of MNPH2 is due to the partly absorption of melanin nanoparticles, and only a low laser

power was used to induce fluorescence. To further evaluate the photoacoustic performance, the PA signals of MNPH2 solutions of different concentrations were obtained under 760 nm excitation (Figure 2H, inset). Clearly, the signal intensity increased gradually with increasing concentration. The photoacoustic signal was plotted against concentration, and the graph showed there was a linear concentration-dependent increase. The highly linear relationship indicates the suitability of the molecule for PA imaging. Therefore, the excellent NIR-II fluorescence and photoacoustic capacities of MNPH2 suggested it would be an excellent NIR-II fluorescence/PA dual-modal contrast agent.

Photothermal Performance of MNPH2

Considering the strong NIR absorption, the photothermal performance of MNPH2 was explored in vitro. Various concentrations of MNPH2 and laser power densities were used to investigate the photothermal conversion effect. The differences in temperature of the photothermal nano-agent at different conditions were intuitively visualized with the infrared thermal images. As presented in Figure 3A and B, we monitored the real-time infrared thermal images and temperature change for 5 min at a series of concentrations (0, 12.5, 25, 50, 100, 200 μg/mL) of MNPH2 aqueous solutions. The temperature elevation of MNPH2 appeared to correlate well with the increase in concentration. The temperature measured 200 μg/mL was the highest and reached nearly 63.8 °C at 808 nm under the same irradiation conditions, indicating efficient photothermal conversion. In contrast, the temperature of DI water only increased to 35.9 °C, confirming the photothermal conversion was due to the photothermal effect of MNPH2. The temperature of the MNPH2 solution (200 μg/mL) at 1.0 W/cm^2 irradiation increased to 71.4 °C, which was higher than that at 0.25, 0.5, or 0.75 W/cm^2 (Figure 3C). The temperature differences induced by the various laser power densities (0.25, 0.5, 0.75, 1.0 W/cm^2) were visualized using infrared thermal images (Figure S5). Based on the heating and cooling curves of MNPH2 at 100 μg/mL before and after 15 min of continuous laser irradiated (Figure 3D), and the linear time data and –lnθ described in Figure 3E, the photothermal conversion efficiency of the MNPH2 was calculated to be about 25.7%, which was higher than the 18.4% recorded for MNP in our previous report.[33] Photothermal stability is another important parameter for evaluating the photothermal agents.[3,53] The MNPH2 solution was exposed to an 808

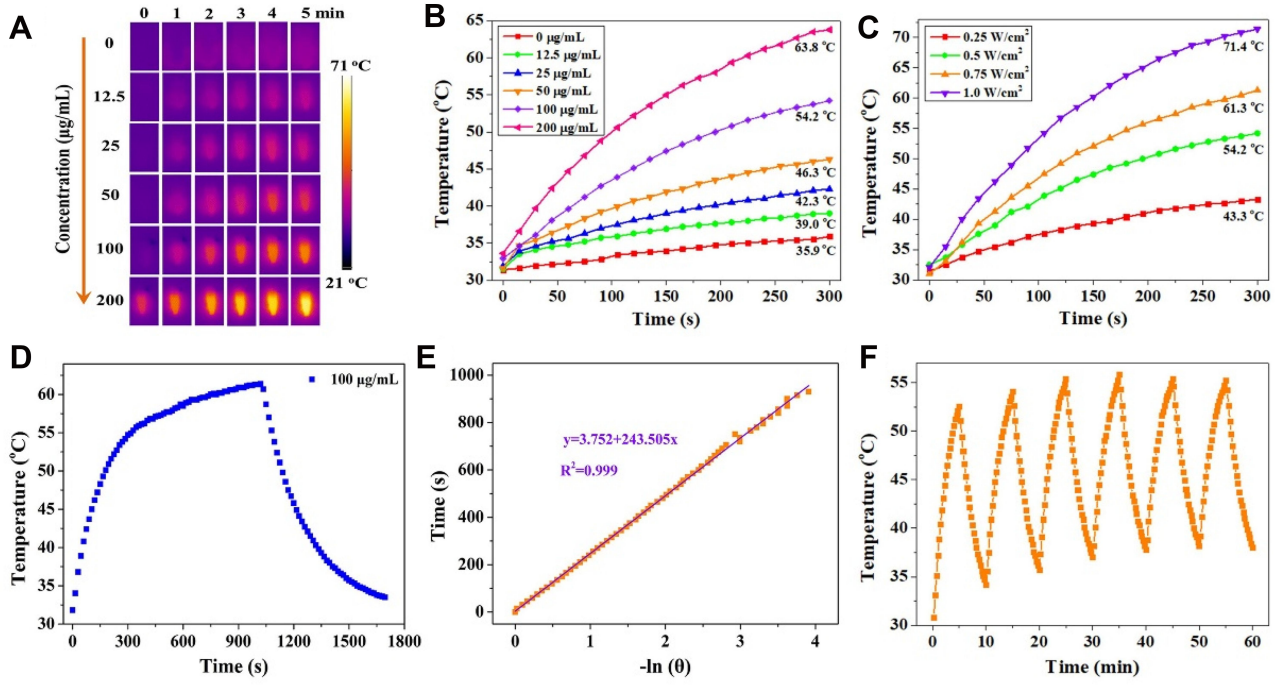

Figure 3 The photothermal capacity of MNPH2 solution. (**A**) Concentration-dependent thermal infrared images of MNPH2 solutions within 5 min under 808 nm laser irradiation (0.5 W/cm^2). (**B**) Temperature change curves of a series of MNPH2 solutions with different concentrations recorded with 808 nm laser irradiation (0.5 W/cm^2). (**C**) Temperature variation curves of MNPH2 solutions under different laser power densities (808 nm, 0.25, 0.5, 0.75, and 1.0 W/cm^2) at 100 μg/mL. (**D**) The heating and cooling curves of MNPH2 aqueous solution (100 μg/mL) measured with irradiation of 808 nm laser (0.5 W/cm^2). (**E**) The linear time data and –lnθ acquired from the cooling period of Figure 3D. The time constant for heat transfer of the MNPH2 was calculated to be 243 s. (**F**) Photothermal stability of MNPH2 (100 μg/mL) in DI water upon irradiation for six cycles (808 nm, 0.5 W/cm^2).

nm laser at a power density of 0.5 W/cm^2 to measure the heating/cooling cycles (Figure 3F). The heating process showed negligible temperature elevation after six continuous off/on cycles of the laser. The satisfactory photothermal performance of MNPH2, including high photothermal conversion efficiency and good optical stability, make it suitable for killing tumor cells.

Cell Experiments

A standard CCK-8 assay with Hep-2 cells was used to evaluate the cytotoxicity of MNPH2. As seen from Figure 4A, we discovered that MNPH2 exhibited nearly 100% cell viability, even at 800 μg/mL, suggesting excellent biocompatibility. The NIR-II fluorescence/PA images of MNPH2 at the cellular level are shown in Figure 4B and C. Distinct NIR-II fluorescence and PA signals were observed in the Hep-2 cells, indicating successful cellular uptake and favorable dual-modal imaging performance. By utilizing the fluorescence of MNPH2 in the visible spectrum (Figure S2), CLSM was used to investigate the internalization of MNPH2 by Hep-2 cells. As shown in Figure 4D, there was the nucleus stained with DAPI is blue and there was a large amount of MNPH2, represented by red fluorescence in the cytoplasm, suggesting that MNPH2 entered Hep-2 cells.

Encouraged by the excellent photothermal capability of MNPH2 solution, we evaluated the efficacity of in vitro thermal ablation of human laryngeal cancer Hep2 cells using MNPH2. As seen from the standard CCK-8 assay (Figure 4A), under laser irradiation, high photothermal cytotoxicity was observed when Hep2 cells were treated

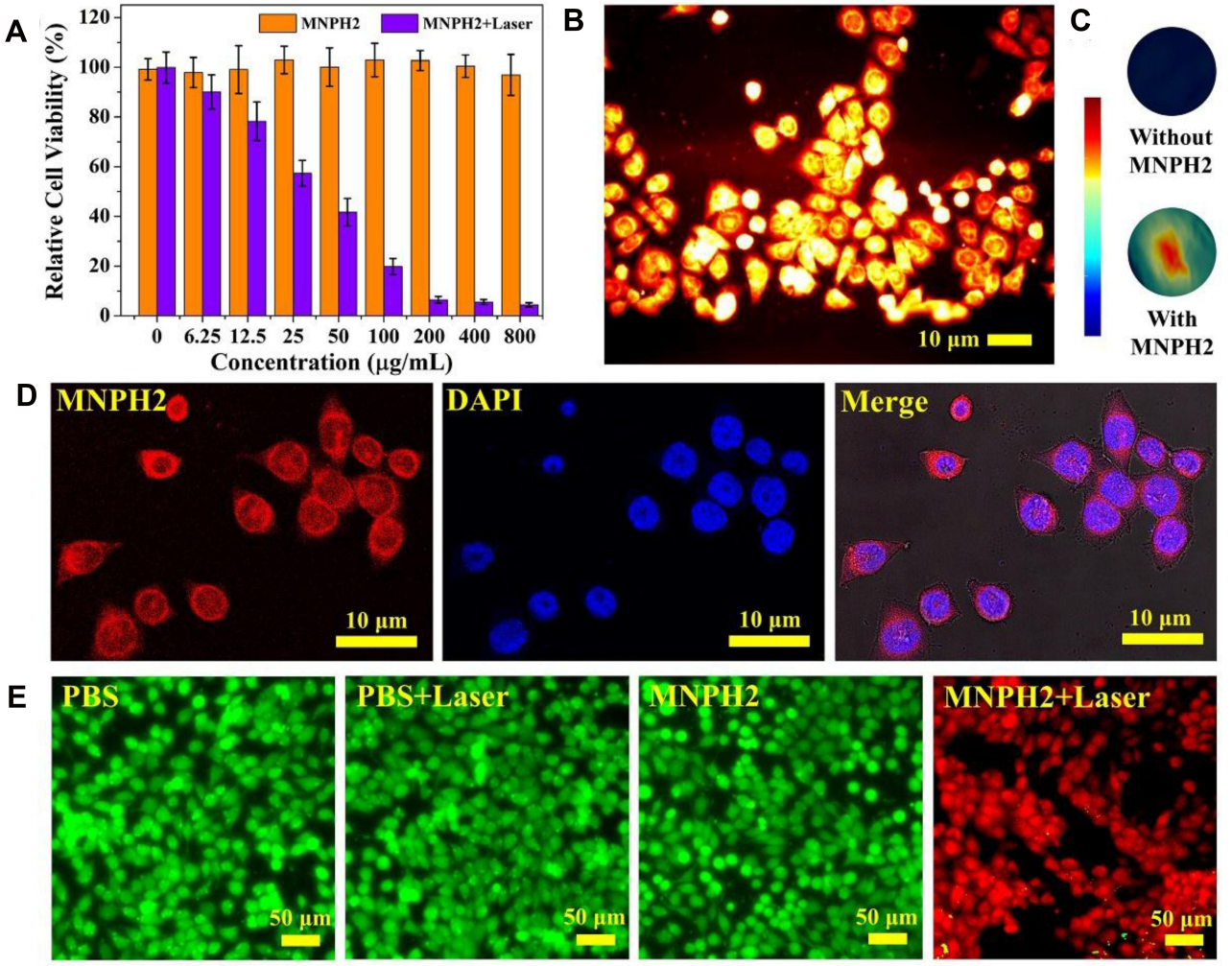

Figure 4 Cell experiments. (**A**) Cell viability of Hep-2 cells incubated with various concentrations of MNPH2 with or without irradiation (808 nm, 0.75 W/cm^2, 5 min). (**B**) NIR-II fluorescence images of Hep-2 cells treated with MNPH2 (100 μg/mL). Scale bar=10 μm. (**C**) PA images of Hep-2 cells treated without and with MNPH2 (100 μg/mL). (**D**) CLSM images for cell internalization. MNPH2 was red and the cell nucleus was stained blue. Scale bar: 10 μm. (**E**) Fluorescence images of Hep-2 cells stained with Calcein-AM (green for live cells) and PI (red for dead cells): PBS, PBS + Laser, MNPH2, and MNPH2 + Laser. Scale bar = 50 μm.

with different concentrations of MNPH2. There was a distinct and remarkable increase in the damage to cell viability with increasing concentrations. Compared with the percentage viability observed with no laser excitation, the cell viability was less than 20% at an MNPH2 concentration of 100 μg/mL. The potent photothermal effect of MNPH2 supports its use as an active PTT agent. To further demonstrate the thermal ablation effect of MNPH2 in vitro, staining experiments with calcein acetoxymethyl ester/propidium iodide (calcein-AM/PI) were further performed to examine the cell death induced by photothermal nano-agents mediated PTT. Hep-2 cells incubated with or without MNPH2 and irradiation were employed to directly observe cell survival after stained with calcein-AM/PI double staining. The dead cells lit up with green fluorescence, while the living cells showed as red. As shown in Figure 4E, we detected strong green fluorescence in the PBS, PBS plus laser, and MNPH2 only group, indicating that most of the cells were viable. With MNPH2 and laser irradiation, a large amount of red fluorescent signal appeared, suggesting a high cell mortality rate, which was attributed to local hyperthermia induced by MNPH2. Taking the above results into consideration, we found it noteworthy that MNPH2 induced a favorable photothermal-response behavior and anti-tumor effect in vitro.

NIR-II Fluorescence/PA Dual-Modal Imaging in vivo

Inspired by the good biocompatibility and outstanding NIR-II fluorescence/PA performance of MNPH2 in vitro, we evaluated the biodistribution and tumor accumulation of the nanoprobe by intravenously administering Hep-2 cell-bearing mice with 200 μL of 800 μg/mL MNPH2. NIR-II fluorescence images were then acquired at designated time points (2 h, 4 h, 8 h, 12 h, and 24 h). As shown in Figure 5A, the tumor was clearly visible in the bright field. After irradiation with 808 laser diode, the tumors became light at 2 h, subsequently, the fluorescence signal gradually increased and reached the maximum at 8 h post-injection, suggesting the MNPH2 nanoprobe effectively accumulated in tumors via the EPR effect. Notably, the fluorescence intensity exhibited a gradual decline 8 h after injection but was still clearly visible in the tumor at 24 h post-injection. Region-of-interest measurements showed that the NIR-II signal ratio between the tumor and background at 8 h was approximately 130.2 ± 6.6 (Figure 5C), indicating the optimal time point for PPT was 8 h. The whole-body NIR-II fluorescent images of mice at 8 h in the lateral and supine position are provided in Figure S6. Strong fluorescence signals were seen in the liver and intestine, indicating the nanoparticles are mainly excreted through hepatoenteric metabolism. After euthanasia, the tumor and major organs were collected for ex vivo NIR-II fluorescence imaging (Figure S7). The strongest NIR-II fluorescence signal was detected in liver tissue followed by kidney, tumor, lung, spleen, and heart, confirming that the MNPH2 is metabolized through hepatobiliary system. The quantitative analysis of each tissue, illustrated in Figure S7B, further supported the above results. After injected with MNPH2, the tumors could be clearly detected with ultra-high spatial resolution and sensitivity, which indicates MNPH2 is a promising candidate in vivo for NIR-II fluorescence imaging agent.

The PA signals were recorded at predetermined time points under 680–980 nm laser excitation. As shown in Figure 5B, the PA signals at the tumor site gradually increased as time progressed and peaked 8 h after MNPH2 injection. Subsequently, the PA signals weakened over time as a result of the in vivo excretion of MNPH2 and showed a similar accumulation in the tumors with NIR-II fluorescence-retention performance (Figure 5D). PA imaging combines ultrasonic and optical characteristics with better tissue contrast, higher spatial resolution, and deeper depth of penetration than traditional ultrasound and optical imaging.[42] Owing to the diminished photon scattering and tissue autofluorescence, NIR-II fluorescence imaging enables the capture of non-invasive, real-time, and whole-body images with improved spatial resolution and high signal-to-background ratios. The dynamic accumulation of NIR-Ⅱ fluorescence and PA in tumor areas were quantitatively analyzed, and the results shown in Figure 5C and D were consistent with the imaging information. The integration of NIR-Ⅱ fluorescence and PA may provide more comprehensive tumor information and help to optimize photothermal therapeutics. NIR-II fluorescence/PA imaging provides valuable information for both diagnosis and therapeutic administration.

In vivo PTT

Encouraged by the success of MNPH2 as an excellent dual-modal imaging and photothermal agent, we used nude mice bearing Hep-2 tumors to assess the effectiveness of imaging-guided PTT for tumor ablation in vivo. The nude mice were randomly divided into four groups, PBS only, PBS + Laser, MNPH2 only, and MNPH2 + Laser, and intravenously

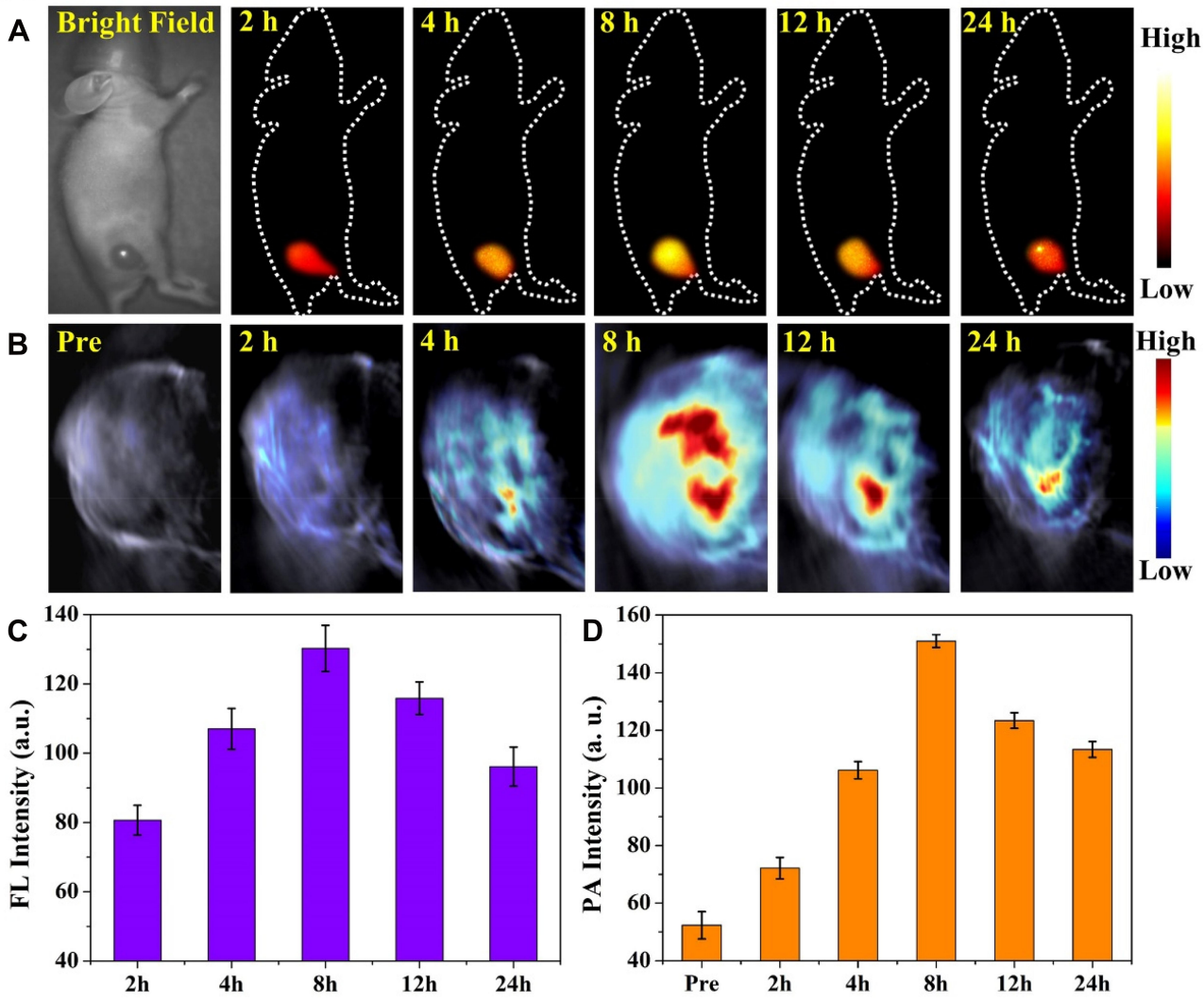

Figure 5 In vivo imaging. Representative time-dependent NIR-II fluorescence images (**A**) and PA images (**B**) in Hep-2 bearing mice treated with MNPH2 at predetermined time points during 24 h. The quantitative analysis intensities of tumor tissue determined by NIR-II fluorescence imaging (**C**) and PA imaging (**D**) at selected time intervals.

injected with 200 μL of PBS or MNPH2 (800 μg/mL). Both NIR-Ⅱ fluorescence and PA imaging indicated that the highest concentration of MNPH2 in the tumor site occurred 8 h after injection. Thus, the two groups of mice were subjected to 5 min of NIR laser irradiation 8 h after post-injection. During the 5 min PTT procedure, whole-body photothermal images of the tumor-bearing nude mice were monitored (Figure 6A), and temperature variation at the tumor site was recorded (Figure 6B). The temperatures of the MNPH2 + laser group increased from 34.2 °C to 59.2 °C; therefore, hyperthermia was achieved to ablate the tumor.[54] In comparison, the temperature of the PBS + laser group reached 41.8 °C within the first 90 s and remained almost unchanged throughout.

The relative tumor volume and body weights of the Hep-2-bearing nude mice treated with PBS only, PBS + Laser, MNPH2 only, and MNPH2 + Laser were recorded every 2 days to evaluate the therapeutic potency. The tumor volumes of three groups (PBS only, PBS + Laser, MNPH2 only) presented a growth trend, especially in the late observation period (Figure 6C). Conversely, there was obvious inhibition of tumor growth in the MNPH2 + laser -treated mice in the first 4 days and no recrudescence during the whole observation period. In addition, there was no significant difference in body weight among these four groups, suggesting that MNPH2 had negligible side effects to the photothermal ablation at local tumor sites (Figure 6D). From H&E staining of the tumor tissue (Figure 6E), we only observed structural damage and dead cells in the group treated with both

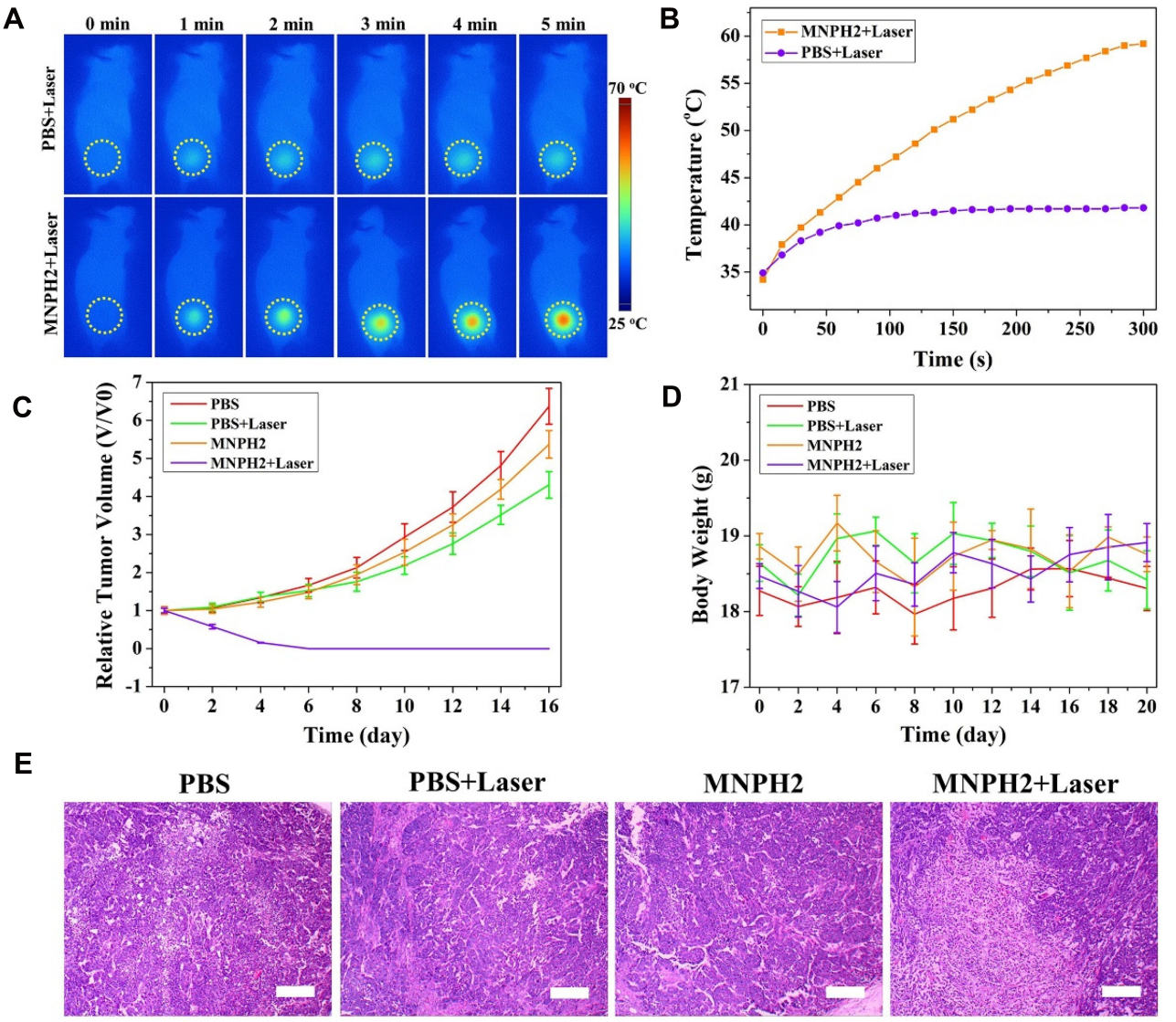

Figure 6 Photothermal evaluation in vivo. (**A**) Whole-body photothermal images of tumor-bearing nude mice intravenously injected with MNPH2 and PBS, followed by (8 h later) an 808 nm laser irradiation within 5 min. (**B**) The temperature variation at the tumor site after photothermal treatment within 5 min. The relative tumors growth curves (**C**) and body weight curves (**D**) of nude mice treated with PBS only, PBS + Laser, MNPH2 only, and MNPH2 + Laser after photothermal treatment. (**E**) Images of H&E analysis from tumor tissues in the above mentioned four groups. (Scale bar=50 μm).

MNPH2 and laser, and this damage was speculatively attributed to cellular necrosis and apoptosis caused by karyopyknosis and fragmentation during the PTT process.[55] These results demonstrated that MNPH2 may serve as a favorable photothermal ablation agent for cancer treatment.

Biosafety Assessment

To further investigate the systemic toxicity of MNPH2 in vivo, the blood and major organs (heart, liver, spleen, lung, and kidney) were harvested from healthy mice after high-dose injection with MNPH2 and PBS, and hematological and histopathological assays were performed. Hematological analysis provided no evidence of liver (ALT and AST), kidney (Scr and BUN), or acute toxicity (Figure 7A). Compared with the PBS group, H&E staining for the MNPH2-treated group showed no apparent necrosis, apoptosis, or another pathology in the major organs (Figure 7B). The hemolysis test verified that MNPH2 did not disrupt erythrocytes or cause hemolysis (Figure S8), suggesting that the MNPH2 nanoparticles are hemocompatible and can be administered intravenously for in vivo cancer treatment. All the above results confirm that MNPH2 possesses excellent biocompatibility and shows negligible systemic toxicity in vivo.

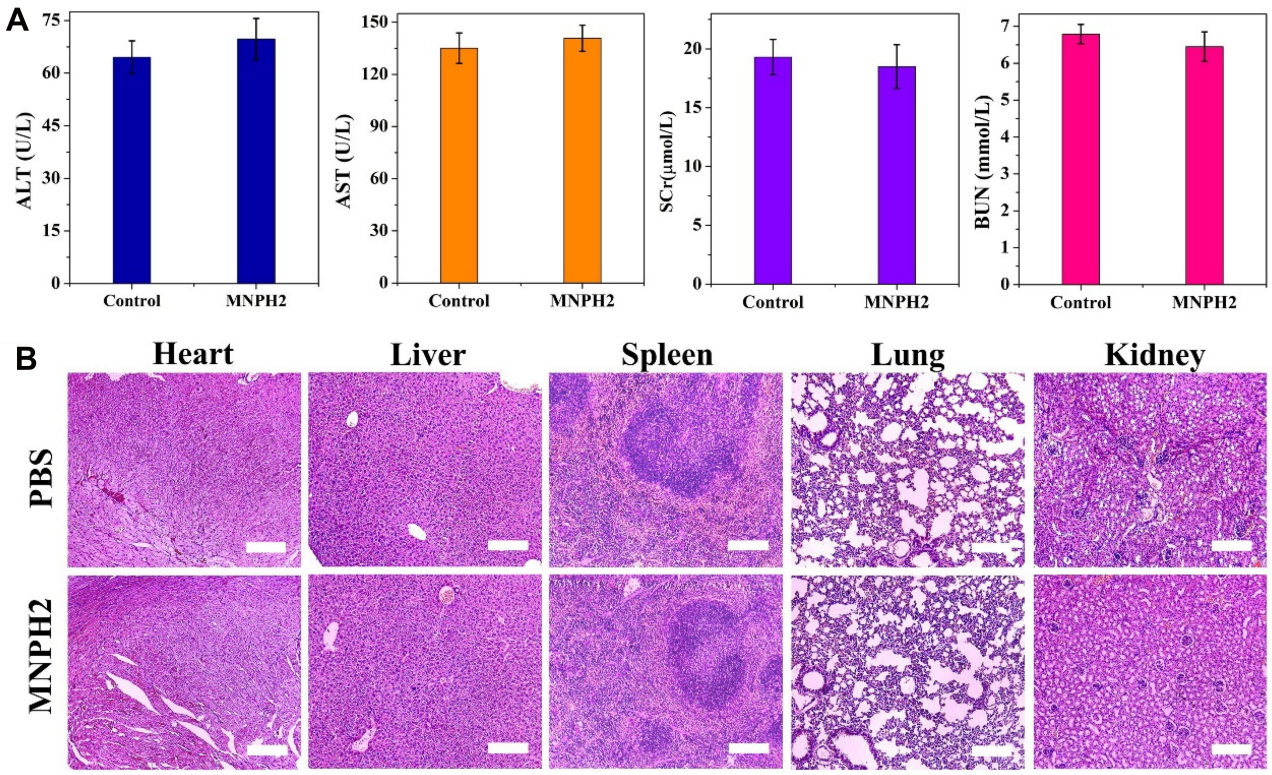

Figure 7 (**A**) Hematological analysis (hepatic function ALT, AST and kidney function Scr, and BUN) of healthy nude mice (n=3) treated with a high-dose of MNPH2 or PBS. (**B**) H&E staining of the major organs collected from healthy mice treated with PBS or high-dose of MNPH2 after 21 days. (scale bar=100 μm).

Conclusions

In summary, we have developed a novel nanoprobe with good physiological stability, excellent NIR-Ⅱ fluorescence and PA imaging performance, and a potent photothermal effect. Toxicity experiments both at the cellular level and in vivo demonstrated that MNPH2 possesses exceptional biocompatibility and minimal systemic toxicity, which are crucial for its biomedical application. Benefiting from dynamic NIR-Ⅱ fluorescence/PA dual-modal imaging, the imaging-guided cancer photothermal treatment provides an excellent therapeutic option for laryngeal cancer. Furthermore, the simple design, combing melanin nanoparticles and NIR fluorescence dye, is highly conducive to expanding its clinical application and optimizes its potential translation into accurate and personalized cancer treatment.

Acknowledgments

This work has been financially supported by the National Natural Science Foundation of China (Grant Nos. 81801767, 81771907 and 82071987), Science and technology innovation team project of Shanxi Province (No. 201705D131026), Engineering Technology Research Center of Shanxi Province No. 201805D121008, Scientific and technological achievements transformation project of Shanxi Province (No. 201704D131006), Laboratory Construction Project of Shanxi Province, the Projects for Local Science and Technology Development Guided by the Central Committee (YDZX20191400002537), Research Project Supported by Shanxi Scholarship Council of China (No.2020-177), Fund Program for the Scientific Activities of Selected Returned Overseas Professionals in Shanxi Province (NO: 20200006). Science and technology innovation project of Shanxi Medical of University (NO. 2020L0192) and Startup Foundation for Doctors of Shanxi Medical University (No. 03201549).

Disclosure

The authors declare no competing financial or non-financial interests.

References

1. Guo ZQ, Park S, Yoon J, Shin I. Recent progress in the development of near-infrared fluorescent probes for bioimaging applications. *Chem Soc Rev.* 2014;43(1):16–29. doi:10.1039/c3cs60271k

2. Li CY, Chen GC, Zhang YJ, et al. Advanced fluorescence imaging technology in the near-infrared-II window for biomedical applications. *J Am Chem Soc*. 2020;142(35):14789–14804. doi:10.1021/jacs.0c07022
3. Wang Y, Zhang W, Sun P, et al. A novel multimodal NIR-II nanoprobe for the detection of metastatic lymph nodes and targeting chemo-photothermal therapy in oral squamous cell carcinoma. *Theranostics*. 2019;9(2):391–404. doi:10.7150/thno.30268
4. Guo B, Feng Z, Hu D, et al. Precise deciphering of brain vasculatures and microscopic tumors with dual NIR-II fluorescence and photoacoustic imaging. *Adv Mater*. 2019;31(30):e1902504. doi:10.1002/adma.201902504
5. Antaris AL, Chen H, Cheng K, et al. A small-molecule dye for NIR-II imaging. *Nat Mater*. 2016;15(2):235–242. doi:10.1038/nmat4476
6. Li XL, Jiang MY, Li YB, Xue ZL, Zeng SJ, Liu HR. 808 nm laser-triggered NIR-II emissive rare-earth nanoprobes for small tumor detection and blood vessel imaging. *Mat Sci Eng C-Mater*. 2019;100:260–268. doi:10.1016/j.msec.2019.02.106
7. Li C, Cao L, Zhang Y, et al. Preoperative detection and intraoperative visualization of brain tumors for more precise surgery: a new dual-modality MRI and NIR nanoprobe. *Small*. 2015;11(35):4517. doi:10.1002/smll.201500997
8. Zhang Q, Zhou H, Chen H, et al. Hierarchically nanostructured hybrid platform for tumor delineation and image-guided surgery via NIR-II fluorescence and PET bimodal imaging. *Small*. 2019;15(45):e1903382. doi:10.1002/smll.201903382
9. Shen Y, Lifante J, Ximendes E, et al. Perspectives for Ag2S NIR-II nanoparticles in biomedicine: from imaging to multifunctionality. *Nanoscale*. 2019;11(41):19251–19264. doi:10.1039/c9nr05733a
10. Li C, Li W, Liu H, et al. An activatable NIR-II nanoprobe for in vivo early real-time diagnosis of traumatic brain injury. *Angew Chem Int Ed Engl*. 2020;59(1):247–252. doi:10.1002/anie.201911803
11. Li Y, Bai G, Zeng S, Hao J. Theranostic carbon dots with innovative NIR-II emission for in vivo renal-excreted optical imaging and photothermal therapy. *ACS Appl Mater Interfaces*. 2019;11(5):4737–4744. doi:10.1021/acsami.8b14877
12. Gong H, Peng R, Liu Z. Carbon nanotubes for biomedical imaging: the recent advances. *Adv Drug Deliver Rev*. 2013;65(15):1951–1963. doi:10.1016/j.addr.2013.10.002
13. Welsher K, Sherlock SP, Dai HJ. Deep-tissue anatomical imaging of mice using carbon nanotube fluorophores in the second near-infrared window. *P Natl Acad Sci USA*. 2011;108(22):8943–8948. doi:10.1073/pnas.1014501108
14. He SQ, Chen S, Li DF, et al. High affinity to skeleton rare earth doped nanoparticles for near-infrared II imaging. *Nano Lett*. 2019;19(5):2985–2992. doi:10.1021/acs.nanolett.9b00140
15. Zhang X, He SQ, Ding BB, et al. Cancer cell membrane-coated rare earth doped nanoparticles for tumor surgery navigation in NIR-II imaging window. *Chem Eng J*. 2020;385:123959. doi:10.1016/j.cej.2019.123959
16. Wang Y, Jiang L, Zhang Y, et al. Fibronectin-targeting and cathepsin B-activatable theranostic nanoprobe for MR/Fluorescence imaging and enhanced photodynamic therapy for triple negative breast cancer. *ACS Appl Mater Interfaces*. 2020;12(30):33564–33574. doi:10.1021/acsami.0c10397
17. Yao D, Wang Y, Zou R, et al. Molecular engineered squaraine nanoprobe for NIR-II/Photoacoustic imaging and photothermal therapy of metastatic breast cancer. *ACS Appl Mater Interfaces*. 2020;12(4):4276–4284. doi:10.1021/acsami.9b20147
18. Yang Y, Fan X, Li L, et al. Semiconducting polymer nanoparticles as theranostic system for near-infrared-II fluorescence imaging and photothermal therapy under safe laser fluence. *ACS Nano*. 2020;14(2):2509–2521. doi:10.1021/acsnano.0c00043
19. Zhu S, Tian R, Antaris AL, Chen X, Dai H. Near-infrared-II molecular dyes for cancer imaging and surgery. *Adv Mater*. 2019;31(24):e1900321. doi:10.1002/adma.201900321
20. Sun Y, Ding M, Zeng X, et al. Novel bright-emission small-molecule NIR-II fluorophores for in vivo tumor imaging and image-guided surgery. *Chem Sci*. 2017;8(5):3489–3493. doi:10.1039/c7sc00251c
21. Zhang XD, Wang H, Antaris AL, et al. Traumatic brain injury imaging in the second Near-Infrared window with a molecular fluorophore. *Adv Mater*. 2016;28(32):6872–6879. doi:10.1002/adma.201600706
22. Gouyon JB, Torrado A, Guignard JP. Renal effects of d-tubocurarine and pancuronium in the newborn rabbit. *Biol Neonate*. 1988;54(4):218–223. doi:10.1159/000242855
23. Sun Y, Qu C, Chen H, et al. Novel benzo-bis(1,2,5-thiadiazole) fluorophores for in vivo NIR-II imaging of cancer. *Chem Sci*. 2016;7(9):6203–6207. doi:10.1039/c6sc01561a
24. Sun Y, Zeng X, Xiao Y, et al. Novel dual-function near-infrared II fluorescence and PET probe for tumor delineation and image-guided surgery. *Chem Sci*. 2018;9(8):2092–2097. doi:10.1039/c7sc04774f
25. Zhang R, Xu Y, Zhang Y, et al. Rational design of a multifunctional molecular dye for dual-modal NIR-II/photoacoustic imaging and photothermal therapy. *Chem Sci*. 2019;10(36):8348–8353. doi:10.1039/c9sc03504d
26. Yang Q, Ma Z, Wang H, et al. Rational design of molecular fluorophores for biological imaging in the NIR-II window. *Adv Mater*. 2017;29(12):e1605497. doi:10.1002/adma.201605497
27. Hong G, Zou Y, Antaris AL, et al. Ultrafast fluorescence imaging in vivo with conjugated polymer fluorophores in the second near-infrared window. *Nat Commun*. 2014;5:4206. doi:10.1038/ncomms5206
28. Zhang X, Xi Z, Machuki JO, et al. Gold cube-in-cube based oxygen nanogenerator: a theranostic nanoplatform for modulating tumor microenvironment for precise chemo-phototherapy and multimodal imaging. *ACS Nano*. 2019;13(5):5306–5325. doi:10.1021/acsnano.8b09786
29. Yao Y, Zhao D, Li N, et al. Multifunctional Fe3O4@Polydopamine@DNA-fueled molecular machine for magnetically targeted intracellular Zn(2+) imaging and fluorescence/MRI guided photodynamic-photothermal therapy. *Anal Chem*. 2019;91(12):7850–7857. doi:10.1021/acs.analchem.9b01591
30. Wu J, Li N, Yao Y, et al. DNA-stabilized silver nanoclusters for label-free fluorescence imaging of cell surface glycans and fluorescence guided photothermal therapy. *Anal Chem*. 2018;90(24):14368–14375. doi:10.1021/acs.analchem.8b03837
31. Zhang X, Ong'achwa Machuki J, Pan W, et al. Carbon nitride hollow theranostic nanoregulators executing laser-activatable water splitting for enhanced ultrasound/fluorescence imaging and cooperative phototherapy. *ACS Nano*. 2020;14(4):4045–4060. doi:10.1021/acsnano.9b08737
32. Liu H, Yang Y, Liu Y, et al. Melanin-like nanomaterials for advanced biomedical applications: a versatile platform with extraordinary promise. *Adv Sci (Weinh)*. 2020;7(7):1903129. doi:10.1002/advs.201903129
33. Sun J, Xu W, Li L, et al. Ultrasmall endogenous biopolymer nanoparticles for magnetic resonance/photoacoustic dual-modal imaging-guided photothermal therapy. *Nanoscale*. 2018;10(22):10584–10595. doi:10.1039/c8nr01215f
34. Fan Q, Cheng K, Hu X, et al. Transferring biomarker into molecular probe: melanin nanoparticle as a naturally active platform for multimodality imaging. *J Am Chem Soc*. 2014;136(43):15185–15194. doi:10.1021/ja505412p
35. Zhang R, Fan Q, Yang M, et al. Engineering melanin nanoparticles as an efficient drug-delivery system for imaging-guided chemotherapy. *Adv Mater*. 2015;27(34):5063–5069. doi:10.1002/adma.201502201

36. Chen A, Sun J, Liu S, et al. The effect of metal ions on endogenous melanin nanoparticles used as magnetic resonance imaging contrast agents. *Biomater Sci*. 2020;8(1):379–390. doi:10.1039/c9bm01580a
37. Varghese L, Mathew J, John S, Job A. Treatment of advanced carcinoma of the larynx and hypopharynx with laser followed by external radiotherapy. *Iran J Otorhinolaryngol*. 2017;29(94):247–253.
38. Janoray G, Pointreau Y, Alfonsi M, et al. Induction chemotherapy followed by cisplatin or cetuximab concomitant to radiotherapy for laryngeal/hypopharyngeal cancer: long-term results of the TREMPLIN randomised GORTEC trial. *Eur J Cancer*. 2020;133:86–93. doi:10.1016/j.ejca.2020.04.009
39. Fan W, Yung B, Huang P, Chen X. Nanotechnology for multimodal synergistic cancer therapy. *Chem Rev*. 2017;117(22):13566–13638. doi:10.1021/acs.chemrev.7b00258
40. Liu Y, Bhattarai P, Dai Z, Chen X. Photothermal therapy and photoacoustic imaging via nanotheranostics in fighting cancer. *Chem Soc Rev*. 2019;48(7):2053–2108. doi:10.1039/c8cs00618k
41. Zeng X, Xiao Y, Lin J, et al. Near-Infrared II dye-protein complex for biomedical imaging and imaging-guided photothermal therapy. *Adv Healthc Mater*. 2018;7(18):e1800589. doi:10.1002/adhm.201800589
42. Chen Q, Wen J, Li H, Xu Y, Liu F, Sun S. Recent advances in different modal imaging-guided photothermal therapy. *Biomaterials*. 2016;106:144–166. doi:10.1016/j.biomaterials.2016.08.022
43. Yu N, Li J, Wang Z, et al. Blue Te nanoneedles with strong NIR photothermal and laser-enhanced anticancer effects as "All-in-One" nanoagents for synergistic thermo-chemotherapy of tumors. *Adv Healthcare Mater*. 2018;7(21):e1800643. doi:10.1002/adhm.201800643
44. Chen H, Zhang J, Chang K, et al. Highly absorbing multispectral near-infrared polymer nanoparticles from one conjugated backbone for photoacoustic imaging and photothermal therapy. *Biomaterials*. 2017;144:42–52. doi:10.1016/j.biomaterials.2017.08.007
45. Cheng K, Chen H, Jenkins CH, et al. Synthesis, characterization, and biomedical applications of a targeted dual-modal Near-Infrared-II fluorescence and photoacoustic imaging nanoprobe. *ACS Nano*. 2017;11(12):12276–12291. doi:10.1021/acsnano.7b05966
46. Miao Q, Pu K. Organic semiconducting agents for deep-tissue molecular imaging: second near-infrared fluorescence, self-luminescence, and photoacoustics. *Adv Mater*. 2018;30(49):e1801778. doi:10.1002/adma.201801778
47. Yao D, Yang S, Wang Y, et al. An ALP-activatable and mitochondria-targeted probe for prostate cancer-specific bimodal imaging and aggregation-enhanced photothermal therapy. *Nanoscale*. 2019;11(13):6307–6314. doi:10.1039/c9nr00913b
48. Sun J, Li X, Chen A, et al. A dual-modality MR/PA imaging contrast agent based on ultrasmall biopolymer nanoparticles for orthotopic hepatocellular carcinoma imaging. *Int J Nanomedicine*. 2019;14:9893–9904. doi:10.2147/IJN.S219794
49. Xing R, Zou Q, Yuan C, Zhao L, Chang R, Self-Assembling endogenous biliverdin as a versatile near-infrared photothermal nanoagent for cancer theranostics. *Adv Mater*. 2019;31(16):e1900822. doi:10.1002/adma.201900822
50. Sadeghi AR, Nokhasteh S, Molavi AM, Khorsand-Ghayeni M, Naderi-Meshkin H, Mahdizadeh A. Surface modification of electrospun PLGA scaffold with collagen for bioengineered skin substitutes. *Mater Sci Eng C Mater Biol Appl*. 2016;66:130–137. doi:10.1016/j.msec.2016.04.073
51. Sahoo B, Devi KSP, Sahu SK, et al. Facile preparation of multifunctional hollow silica nanoparticles and their cancer specific targeting effect. *Biomater Sci*. 2013;1(6):647–657. doi:10.1039/c3bm00007a
52. Li T, Li C, Ruan Z, et al. Polypeptide-conjugated second near-infrared organic fluorophore for image-guided photothermal therapy. *ACS Nano*. 2019;13(3):3691–3702. doi:10.1021/acsnano.9b00452
53. Yang T, Tang Y, Liu L, et al. Size-dependent Ag2S nanodots for second Near-Infrared fluorescence/photoacoustics imaging and simultaneous photothermal therapy. *ACS Nano*. 2017;11(2):1848–1857. doi:10.1021/acsnano.6b07866
54. Hu X, Lu F, Chen L, et al. Perylene diimide-grafted polymeric nanoparticles chelated with Gd(3+) for photoacoustic/T1-weighted magnetic resonance imaging-guided photothermal therapy. *ACS Appl Mater Interfaces*. 2017;9(36):30458–30469. doi:10.1021/acsami.7b09633
55. Liu T, Zhang MK, Liu WL, et al. Metal ion/tannic acid assembly as a versatile photothermal platform in engineering multimodal nanotheranostics for advanced applications. *Acs Nano*. 2018;12(4):3917–3927. doi:10.1021/acsnano.8b01456